



Trans. Nonferrous Met. Soc. China 35(2025) 3368-3382

Transactions of **Nonferrous Metals** Society of China

www.tnmsc.cn



# Influencing mechanism of laser specific energy on tribological properties of high performance Ti-Al/WC composite coating

Xin-meng SUI<sup>1,2#</sup>, Yi-tao WENG<sup>2#</sup>, Jian LU<sup>2,3</sup>, Lin ZHANG<sup>1</sup>, Wei-ping ZHANG<sup>1</sup>

1. Key Laboratory of Solidification Control and Digital Preparation Technology (Liaoning Province), School of Materials Science and Engineering, Dalian University of Technology, Dalian 116024, China;

2. Guangxi Key Laboratory of Manufacturing Systems and Advanced Manufacturing Technology, School of Mechanical and Electrical Engineering, Guilin University of Electronic Technology, Guilin 541004, China;

3. National Engineering Research Center for Special Mineral Material,

China Nonferrous Metals (Guilin) Geology and Mining Co., Ltd., Guilin 541004, China

Received 31 January 2024; accepted 15 November 2024

Abstract: Laser specific energy significantly impacts the quality of composite coatings. Ti-Al/WC coatings were prepared on the TC21 alloy through laser cladding with specific energy ranging from 66.7 to 133.3 J/mm<sup>2</sup>. The results indicate that the composite coatings primarily comprised Ti<sub>2</sub>AlC, α<sub>2</sub>-Ti<sub>3</sub>Al, γ-TiAl, TiC, and W phases. A gradual increase in the relative intensity of the diffraction peaks of Ti<sub>2</sub>AlC, α<sub>2</sub>-Ti<sub>3</sub>Al, and TiC appeared with the increase of specific energy. When the specific energy was 116.7 J/mm<sup>2</sup>, the Ti-Al/WC coated alloy achieved a maximum microhardness of HV<sub>0.2</sub>766.3, which represented an increase of 1.96 times compared with TC21 alloy, and the minimum wear rate decreased dramatically. Much improvement in tribological properties was attained through the fine-grained strengthening of the  $(\alpha_2+\gamma)$  matrix and the dispersion strengthening of self-lubricating Ti<sub>2</sub>AlC and intertwining TiC. This study provides valuable insights for the development of high-performance Ti-Al composite coatings. Key words: laser specific energy; Ti-Al/WC coating; TC21 alloy; Ti<sub>2</sub>AlC; tribological properties

# 1 Introduction

Titanium and its alloys are essential structural and biomedical materials used in aerospace, automobiles, and shipbuilding industries [1,2]. Among them, the TC21 titanium alloy, newly developed by the Northwest Institute Non-ferrous Metal Research (China) is widely employed as a significant structural material in the aerospace industry due to its exceptional mechanical properties, including superior toughness, high specific strength, and outstanding damage tolerance [3-6]. However, the durability and functionality of TC21 titanium alloy are severely impeded by its unremarkable hardness and insufficient wear resistance under extremely harsh wear and friction conditions [7,8]. The hardness and wear resistance of the material play a crucial role in evaluating the mechanical reliability and durability of critical structural components such as aircraft fuselage, turbine discs, landing gears, or airfoil joints [9,10].

In response to this demand, mainstream efforts to enhance mechanical properties have been focused on tailoring the microstructure through surface modifying technologies, such as high current pulsed electron beam treatment [11,12],

<sup>#</sup> Xin-meng SUI and Yi-tao WENG contributed equally to this work

physical vapor deposition (PVD) or chemical vapor deposition (CVD) [13,14], laser peening [15], plasma spraying [16], and micro-arc oxidation [17,18]. Among these techniques, laser cladding (LC) is an advanced yet simple and reliable processing technology [19-21]. During the laser cladding process, metal powders are injected into the molten pool generated by the laser on the substrate and rapidly resolidified after melting due to a high cooling rate of approximately 10<sup>3</sup>−10<sup>6</sup> °C/s, which can endow a significantly refined structure to strengthen the coating [22]. Notably, LC is characterized by a concentrated energy density, lower dilution rate, dense and thick coatings, as well as strong metallurgical bonding between the coating and substrate, making it increasingly useful for repairing critical components [23].

At present, extensive research has been conducted on the deposition of ceramic-reinforced metal substrate composite coatings on titanium alloys using LC. A key advantage of these composite coatings is their ability to enhance wear resistance through the synergistic effect between tough metals or alloys and hard ceramic phases [24]. Nitrides [25,26], carbides [19,27], and oxides [28,29] are commonly employed as the reinforcing phases for these coatings. WC particles are viewed as an appropriate material for enhancing the surface properties of titanium alloy due to their exceptional hardness, wear resistance, and a thermal expansion coefficient similar to that of titanium alloys [30]. Since the compatibility between high-hardness ceramic and metal materials is usually poor, the bonding quality of coatings between coating and substrate cannot be ensured [29]. However, incorporating Ti-Al metals as a binder strengthens the interfacial binding of the ceramic phase and the substrate, thereby mitigating residual stress, cracking, and peeling of the coatings [30-32]. Moreover, the hardness and plasticity of the coating can be effectively enhanced through the in-situ formation of Ti-Al intermetallic compounds [33]. During metallurgical reactions, the growth time of intermetallic compounds is influenced by factors such as laser power, scanning speed, and spot diameter, which collectively regulate the laser energy input (maximum temperature, heating rate, and cooling rate) into the molten pool [34]. These parameters can be visually converted into a single

variable known as laser specific energy that affects the microstructure [35]. While some studies have touched upon Ti–Al/WC composite coatings in recent years, there remains a dearth of comprehensive investigations into the influence of specific energy on the microstructure and wear resistance of Ti–Al/WC composite coatings.

Laser specific energy appears to be neglected in studies on LC. Undoubtedly, different materials and processing requirements necessitate varying ranges of laser specific energy, which plays a paramount role in the quality of cladding coating, microstructure, and wear resistance [36]. WENG et al [37] fabricated Co-based composite coating on Ti-6Al-4V titanium alloy using mixture of Co42 and B<sub>4</sub>C powders through laser cladding. Results indicated that the TiC dendrites and TiB particles were refined with a decrease in laser specific energy (from 12.7 to 4.9 kJ/cm<sup>2</sup>). KUMAR et al [38] successfully fabricated a composite coating of cubic boron nitride, TiO<sub>2</sub>, and base Ti-6Al-4V via the laser cladding process. They found that the layer thickness and microhardness are notably affected by variations in laser process parameters. The formation of anti-wear borides and nitrides, which take on various shapes such as needles, cylindrical rods, and short-length dendritic structures, enhances the hardness and wear resistance of the coatings to varying degrees. SUI et al [36] studied the impact of laser specific energy on TiN reinforced Ti<sub>3</sub>Al composite coating, prepared by mixing Ti, Al, and TiN powder. Results revealed that at an optimum specific energy of 58.3 J/mm<sup>2</sup>, the coating exhibited a uniform distribution of TiN and a finer microstructure. Additionally, a core-rim structure was formed within the coating leading to a roughly threefold increase in microhardness compared to the substrate, resulting in tremendously improved wear resistance. Therefore, controlling specific energy is crucial for enhancing the tribological properties of composite coatings, though few studies have explored the effects of specific energy on the properties of Ti-Al/WC coatings.

In this study, Ti-Al/WC coatings were prepared on the TC21 titanium substrate via laser cladding to investigate the relationship between laser specific energy input and wear resistance of the composite coating. The study examined the evolution process of the microstructure under different specific energy inputs by regulating the

phase composition, carbide morphology, and grain size of intermetallic compounds in the coatings. Additionally, the composite coatings were evaluated for microhardness and tribological performance in a comparative manner.

# 2 Experimental

TC21 titanium alloy, with its principal chemical composition detailed in Table 1 (made in the Northwest Institute for Nonferrous Metal Research, China), was selected as the substrate metal. The substrate was cut into dimensions of  $30 \text{ mm} \times 15 \text{ mm} \times 8 \text{ mm}$ , and then polished and cleaned to remove impurities that could affect the coating quality before laser processing. Ti powder (99.9% in purity, ≤48 µm) and Al powder (99.9% in purity, 48-74 µm) were mixed at an atomic ratio of 1:1, with 20 wt.% WC powders (99.9% in purity, particle size <10 µm) added to the mixture as coating material. These alloy powders were evenly blended in an agate mortar under vacuum conditions by mechanical stirring for 0.5 h. Before the laser cladding process, the specimens were dried in a vacuum drying oven at 50 °C for 24 h to eliminate moisture present in the cladding powders and effectively prevent oxidation. To ensure the accuracy in the composition of the mixed powder, the coatings were uniformly fabricated on the test piece using the preplaced powder method. After compacting the mixed powders onto the surface of the TC21 substrate with a special mold, the powder path had a length of 30 mm, a width of 3 mm, and a thickness of approximately 1 mm.

**Table 1** Chemical composition of TC21 (wt.%)

Al	Mo	Cr	Zr	Sn	Nb	Si	О	Ti
6.10	2.60	1.60	1.70	1.93	1.96	0.13	0.09	Bal.

Laser cladding coatings were manufactured using an LDF 4000-100 fiber laser apparatus (Laserline Company, Koblenz, Germany) with a maximum laser power of 6000 W. The spot diameter was 3 mm, defocus amount was 20 mm, and wavelength was 1070 nm. A schematic diagram of the laser cladding process is shown in Fig. 1(a). High-purity argon gas was introduced into the protective box at a rate of 15 L/min during the cladding process to prevent oxidation of the coatings. To assess the factors influencing the evolution of Ti–Al/WC coating, a specific energy

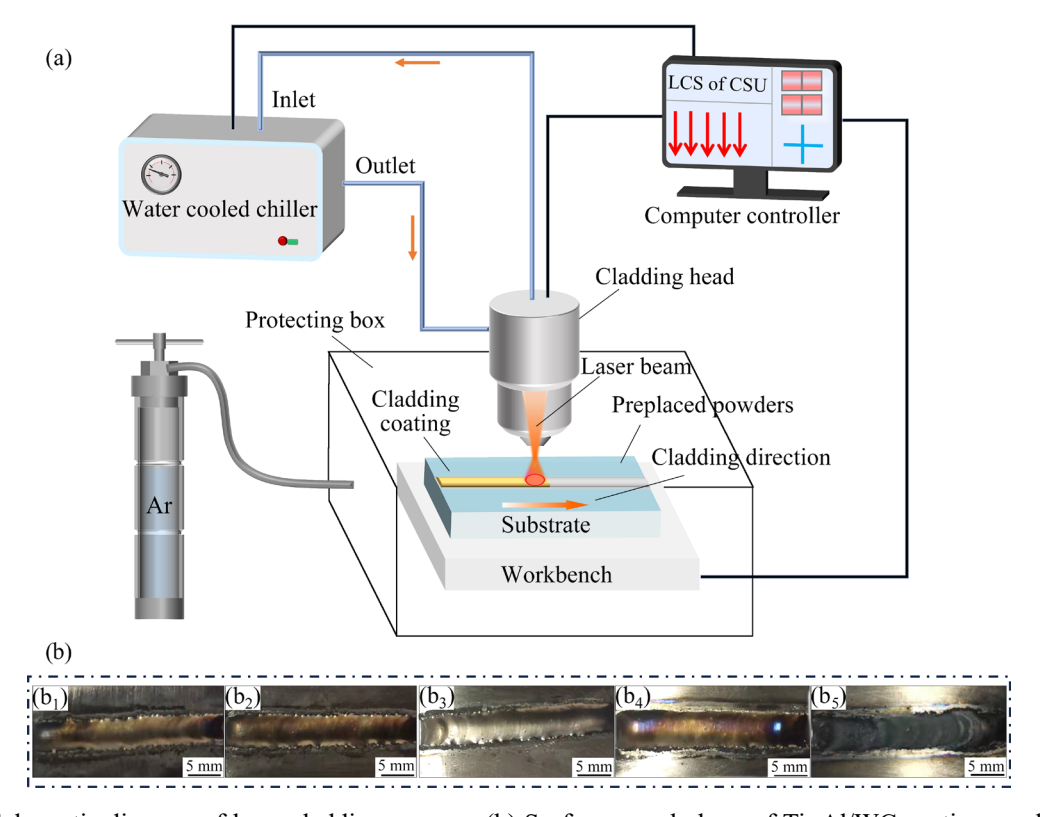


Fig. 1 (a) Schematic diagram of laser cladding process; (b) Surface morphology of Ti–Al/WC coatings under different specific energies: (b<sub>1</sub>)  $66.7 \text{ J/mm}^2$ ; (b<sub>2</sub>)  $80.0 \text{ J/mm}^2$ ; (b<sub>3</sub>)  $100.0 \text{ J/mm}^2$ ; (b<sub>4</sub>)  $116.7 \text{ J/mm}^2$ ; (b<sub>5</sub>)  $133.3 \text{ J/mm}^2$ 

was introduced to quantify the laser heat input from the cladding head to the specimens during laser processing, which can be calculated using the following equation [36]:

$$E = P/(V \cdot D) \tag{1}$$

where E (J/mm<sup>2</sup>) is the specific energy, P (W) is the laser power, V (mm/s) is the scanning speed and D (mm) is the spot diameter. The variations in the specific energy of laser cladding are listed, with samples Nos. 1–5 corresponding to 66.7, 80.0, 100.0, 116.7, and 133.3 J/mm<sup>2</sup>, respectively. The technological parameters of laser cladding are listed in Table 2.

**Table 2** Technological parameters of laser cladding

Comple	Laser	Scanning	Spot	Specific
Sample No.	power,	speed,	diameter,	energy,
NO.	P/W	$V/(\text{mm}\cdot\text{s}^{-1})$	D/mm	$E/(\mathrm{J\cdot mm^{-2}})$
1	1000	5	3	66.7
2	1200	5	3	80.0
3	1200	4	3	100.0
4	1400	4	3	116.7
5	1200	3	3	133.3

After laser cladding treatment, the specimens were wire cut into dimensions of 15 mm  $\times$  15 mm  $\times$ 8 mm perpendicular to the cladding direction. X-ray diffractometry (XRD) (XRD-6000, PANalytical Empyrean, Netherlands) was performed with continuous scanning  $2\theta$  from  $20^{\circ}$  to  $90^{\circ}$  using Cu  $K_{\alpha}$  irradiation at room temperature to identify the phase constituents of the prepared coatings. the cross-sections of the specimens underwent standard mechanical polishing followed by etching with a mixture of deionized HF, HNO<sub>3</sub>, and H<sub>2</sub>O in a volume ratio of 1:2:30 for approximately 10 s at room temperature. The cross-sectional microstructure of the coatings was characterized using scanning electron microscope (SEM) (JSM-7900F, JEOL, Japan) combined with energy dispersive spectrometer (EDS).

The microhardness along the coating depth was measured using a micro-Vickers hardness tester (DHV-1000) under a load of 1.96 N and a load-dwell time of 15 s. To minimize the testing errors, the hardness value was calculated as the average of three test results. The coatings of the specimens were polished by pre-grind prior to the wear test.

The wear test was conducted at room temperature using a CFT-I friction wear tester with a normal load of 9.8 N, a sliding speed of 100 mm/s, a sliding distance of 5 mm, and a duration of 30 min. The friction pair consists of a  $Si_3N_4$  ball with a diameter of 3 mm. To ensure the correctness of the results, the hardness value was taken as the average of measurements at equal depths (with a lateral interval of 50  $\mu$ m). Additionally, after each specimen completed its respective test, the friction pair was replaced. Furthermore, SEM analysis was performed on each worn surface to investigate the wear characteristics of the composite coating.

# 3 Results and discussion

#### 3.1 Macroscopic morphology

When fabricating large-scale industrial high-performance components, the quality of the coating is crucial. The performance of laser cladding coating is significantly affected by the morphology and defects of the cladding layer, including porosity and cracks. Figure 1(b) displays the macroscopic features of the composite coatings under laser cladding with varying specific energy. When the specific energy reached 133.3 J/mm² (Fig. 1(b<sub>5</sub>)), the macroscopic characteristic of composite coatings showed a lack of metallic luster, irregular shape, poor track quality, and a significantly lower cladding height. Other specimens exhibited a high finish, uniform metallic luster, and no obvious defects, as shown in Figs. 1(b<sub>1</sub>-b<sub>4</sub>).

# 3.2 Phase constitution

The XRD diffraction patterns of the composite coatings with different laser specific energies are presented in Fig. 2. Overall phase identification of various laser specific energy shows high similarity. It is evident that the composite coatings primarily consisted of Ti<sub>2</sub>AlC, α<sub>2</sub>-Ti<sub>3</sub>Al, γ-TiAl, TiC, and W phases while also containing a small amount of  $\beta$ -Ti, W<sub>2</sub>C, and WC phases. XRD analysis revealed that as the specific energy increased from 66.7 to 116.7 J/mm<sup>2</sup>, there was a gradual elevation in the relative intensity of the diffraction peaks of Ti<sub>2</sub>AlC, TiC,  $\alpha_2$ -Ti<sub>3</sub>Al, W, and W<sub>2</sub>C, indicating a corresponding rise in the amount of reaction precipitates in coatings. Under the influence of high-energy laser beam, WC particles decarbonized and transformed into W2C due to thermal impact.

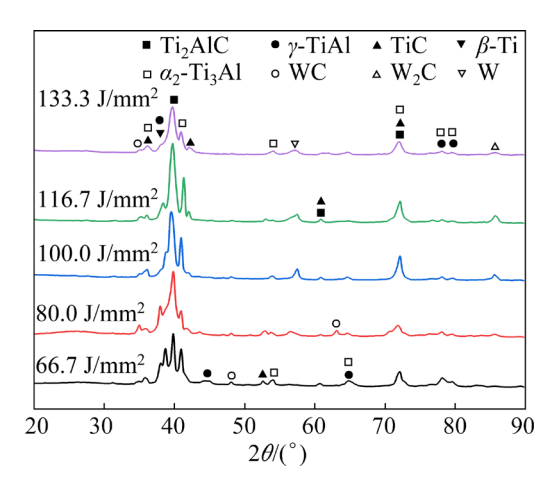


Fig. 2 XRD patterns of Ti-Al/WC coatings prepared under different specific energies

Thus, the dissociative Ti and C easily formed the TiC phase in the molten pool by a chemical reaction because of their high chemical affinity [39,40]. This transformation is evident from the presence of peaks corresponding to  $W_2C$ , W, and TiC in the XRD pattern of the coatings. Furthermore, the intensity of the diffraction peak of WC was relatively weak, indicating the presence of residual unmelted WC particles in composite coatings. Simultaneously, the relative intensity of the main diffraction peaks corresponding to  $Ti_2AlC$  and  $\alpha_2$ - $Ti_3Al$  steadily increased and reached a peak when the specific energy was improved to  $116.7 \text{ J/mm}^2$ . This result can be explained by the fact that with an increase in specific energy, the

solidification and cooling rate of the molten pool slow down, which contributes to the generation of the  $Ti_2AIC$  phase at high heat input.

According to the Ti-Al binary phase diagram [36], when there is a 1:1 atom ratio between Ti and Al, the  $\gamma$ -TiAl should be formed as a major product. However, with the increase of specific energy, the TC21 substrate undergoes melting during the laser cladding process, causing a large number of Ti elements to rush into the molten pool, and resulting in a shift in solidification path towards the left. When the Ti content is high,  $\alpha_2$ -Ti<sub>3</sub>Al becomes the predominant product formed. Once the specific energy reaches 133.3 J/mm<sup>2</sup>, there is a slight decrease in the relative intensity observed for diffraction peaks corresponding to  $\alpha_2$ -Ti<sub>3</sub>Al, TiC, and Ti<sub>2</sub>AlC. This decrease is mainly attributed to high specific energy exceeding the critical value, leading to vigorous interaction between the laser beam and the molten pool, which induces turbulence in the latter and results in liquid droplet splashing. Additionally, TiC [41], W<sub>2</sub>C [42], and Ti<sub>2</sub>AlC phases [43,44] are well-known ceramic phases that exhibit typical characteristics of hard reinforcement or abrasion resistance, which can effectively enhance the microhardness and wear resistance of coatings.

# 3.3 Microstructure

Figures 3(a-e) show the backscattered electron (BSE) images of the Ti-Al/WC coatings prepared

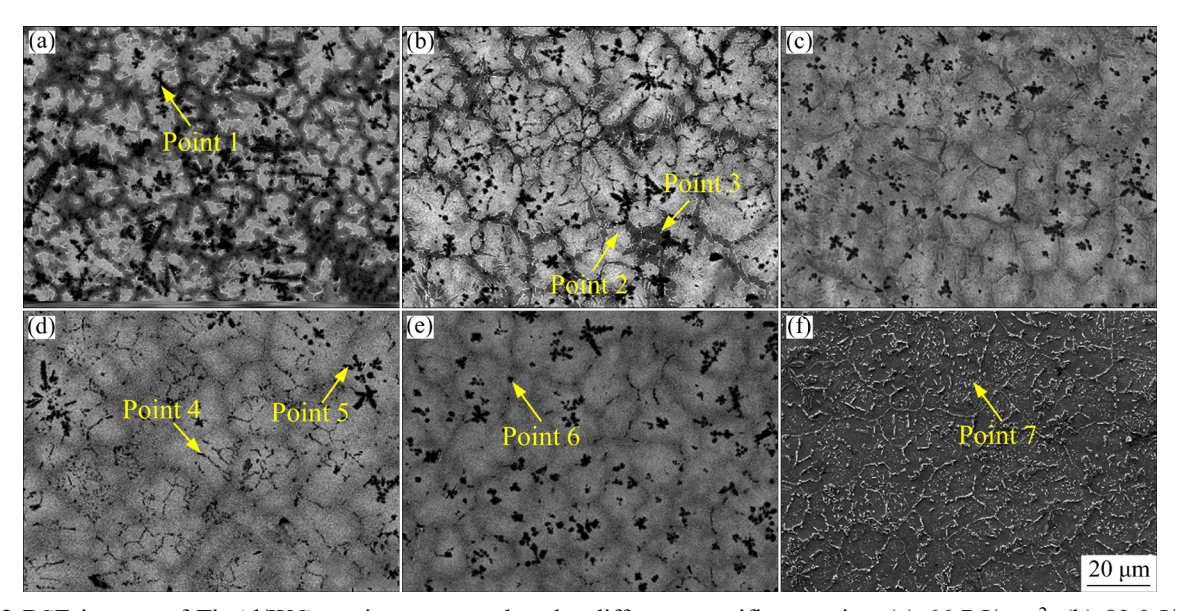


**Fig. 3** BSE images of Ti-Al/WC coatings prepared under different specific energies: (a) 66.7 J/mm<sup>2</sup>; (b) 80.0 J/mm<sup>2</sup>; (c) 100.0 J/mm<sup>2</sup>; (d) 116.7 J/mm<sup>2</sup>; (e) 133.3 J/mm<sup>2</sup>; (f) SEM image of Ti-Al/WC coating prepared with specific energy of 116.7 J/mm<sup>2</sup>

under different specific energies. It can be discovered that the cladding layer is primarily composed of greyish white block phases, grey phases, and numerous black phases. The black phases include dendritic phases (Point 1), petal-like phases, thin strip phases (Point 4), short rod-like phases (Point 5), and granular phases (Point 6). EDS analysis results for these phases are given in Table 3. It can be determined that the greyish white block phases (Point 2) mainly contain Ti and Al elements with an atomic ratio close to 3:2, indicating its presence as an  $(\alpha_2+\gamma)$  lamellar structure in the microstructure [45,46]. The grey phase (Point 3) predominantly contains Ti and Al elements with an atomic ratio close to 1:1, suggesting it is  $\gamma$ -TiAl. EDS results for Points 1, 4, 5, and 6 indicate that the black phases are primarily composed of Ti and C with an atomic ratio of approximately 1:1, identifying them as TiC. Figure 3(f) depicts the morphology of the cladding layer after etching prepared at a specific energy of 116.7 J/mm<sup>2</sup>. Following corrosion treatment, a large amount of white granular phase emerges in the cladding layer. EDS analysis of Point 7 reveals that it mainly consists of Ti, Al, and C elements with an atomic ratio of about 2:1:1. Therefore, the white granular phase is identified as Ti<sub>2</sub>AlC, which is supported by the XRD pattern of the cladding coatings.

In order to further explore the in-situ synthesis mechanism of Ti<sub>2</sub>AlC phase during laser cladding, EDS analysis was conducted on the element

**Table 3** EDS analysis results in different regions (in Fig. 3) of Ti-Al/WC coatings

Point		Possible			
No.	Ti	Al	С	W	phase
1	54.36	0.86	45.48	0.64	TiC
2	48.46	33.64	14.88	2.92	$(\alpha_2+\gamma)$
3	47.69	39.42	11.78	2.20	γ-TiAl
4	45.06	6.53	48.33	0.68	TiC
5	50.24	2.48	47.67	0.73	TiC
6	44.01	1.57	55.86	0.44	TiC
7	52.89	27.68	15.71	2.97	Ti <sub>2</sub> AlC

distribution in Ti-Al/WC coating prepared under a specific energy of 116.7 J/mm<sup>2</sup>, as shown in Fig. 4. According to Figs. 4(a, b), the point scan data revealed an atomic ratio of approximately 2:1:1 for Ti, Al, and C elements in the white granular phase (Point 8), with a small presence of W element. Figures 4(c-f) display EDS mapping images for Ti, Al, C, and W elements, respectively. It can be clearly observed that the white granular phases are enriched with Ti, Al, and C elements, confirming their identification as Ti<sub>2</sub>AlC phases. At the same time, the combination of EDS spectra (Figs. 4(c-f)) with image from Fig. 4(a) revealed distinct elemental segregation in the dendritic and granular phases, with high concentrations of Ti and C elements indicating the presence of TiC. Importantly, the edge regions of TiC phases mainly consisted of Ti<sub>2</sub>AlC, while the coating matrix

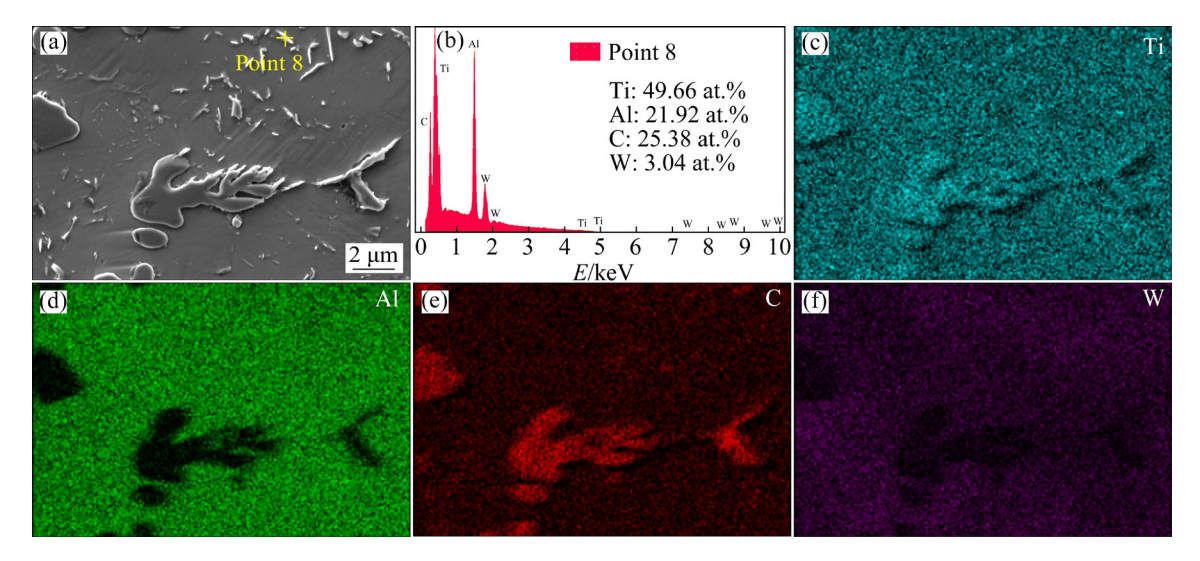


**Fig. 4** EDS mapping of element distribution of part microstructure in Ti–Al/WC coating prepared at specific energy of 116.7 J/mm<sup>2</sup>: (a) SEM image of microstructure; (b) EDS spectrum of Point 8; (c–f) Element distributions of Ti, Al, C, and W, respectively

comprised  $(\alpha_2+\gamma)$  intermetallic compounds. The W atoms were evenly distributed in the  $(\alpha_2+\gamma)$ intermetallic compounds. Moreover, most regions within the coating matrix were covered by growing white granular phases; the Ti<sub>2</sub>AlC phases were embedded centrally within the TiC mesh, as shown in Fig. 3(f). This was further confirmed by XRD diffraction peak, which indicated a predominant presence of the Ti<sub>2</sub>AlC phase. The increased specific energy enhanced the fluidity of the molten pool, promoting the diffusion of Ti and Al atoms and facilitating their interaction with C to form the white granular Ti<sub>2</sub>AlC phase. Due to the rapid cooling rate associated with high laser specific energy, the nucleation of TiC is constrained, and the growth of nucleated TiC primarily occurs through solute redistribution. As a result, the diffusion of certain Al atoms within the coatings leads to the formation of a core-shell structure with TiC as the core and Ti2AlC as the shell. Thus, appropriate specific energy can promote continuous growth of the coating microstructure, resulting in a more homogeneous microstructure and facilitating the emergence of the Ti<sub>2</sub>AlC phase.

To investigate the correlation between specific energy and the TiC phase, the microstructure of the composite coating prepared under varying specific energy conditions was analyzed after corrosion, as shown in Fig. 5. The characteristics of the TiC phase in the coatings varied due to different specific energy. Figures 3(a) and 5(a) show that numerous coarse dendrites of in-situ grown TiC distributed in

the coating. As depicted in Figs. 3(c) and 5(c), when the specific energy reached 100.0 J/mm<sup>2</sup>, these coarse dendrites transformed into a petal-like morphology, resulting in a significant decrease in dendritic TiC. Furthermore, a small amount of granular structure TiC emerged, potentially surrounded by  $\beta$ -Ti to inhibit its growth, thus indicating its presence [47]. As observed in Figs. 3(d) and 5(d), the microstructure of the coating became denser and more uniform as the specific energy was further increased to 116.7 J/mm<sup>2</sup>, which resulted in a considerable rise in the nucleation rate of the coating. Numerous evenly-dispersed TiC thin strip phases formed an interlocking reticular-like structure within the coating, contributing to grain refinement and dispersion strengthening of the TiC phase. Moreover, as the specific energy increased from 66.7 to 116.7 J/mm<sup>2</sup>, the types of  $\gamma$ -TiAl intermetallic compounds and  $(\alpha_2+\gamma)$  lamellar structures tended to merge into  $(\alpha_2+\gamma)$  structures in Figs. 3(a-d) and 5(a-d). Overall, the microstructure underwent gradual refinement.

As shown in Figs. 3(e) and 5(e), the microstructure of the obtained coating transformed drastically with increasing specific energy to 133.3 J/mm<sup>2</sup>. The presence of TiC thin strip phases decreased, while the TiC content increased significantly, transitioning from thin strip phase and short rod-like phase to black dendritic phase and spherical particle phase. Meanwhile, a small amount of petal-like TiC was observed. Previous

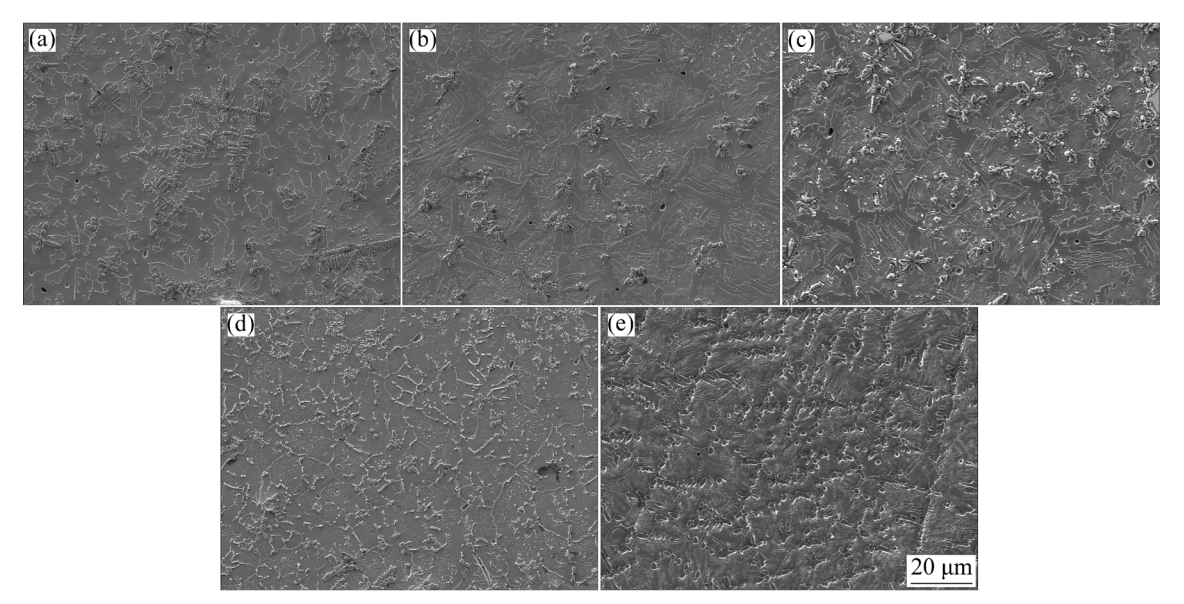


**Fig. 5** SEM images after corrosion of Ti–Al/WC coatings prepared under different specific energies: (a) 66.7 J/mm<sup>2</sup>; (b) 80.0 J/mm<sup>2</sup>; (c) 100.0 J/mm<sup>2</sup>; (d) 116.7 J/mm<sup>2</sup>; (e) 133.3 J/mm<sup>2</sup>

studies have indicated the generation of two types of TiC: eutectic TiC and primary TiC. Primary TiC tends to form dendrites, whereas eutectic TiC primarily appears as short rod-like phase or granular phase [48]. The morphology of TiC is partially attributed to the C content. Initially, as the specific energy increases, the C content also increases, leading to the formation of dendritic and petal-like TiC in the cladding layer. When the C content approaches the eutectic transition point, two factors become influential. First, the intense interaction between the high-energy laser beam and the molten pool causes turbulence, leading to liquid splashing. This results in partial carbon loss due to burning, reducing the C content in the molten pool. Second, laser power significantly impacts the dilution rate of the cladding layer, allowing a large amount of titanium (Ti) from the substrate to enter the molten pool. This dilutes the C content, and TiC becomes surrounded by  $\beta$ -Ti, restricting its growth. Consequently, there is insufficient C content in the molten pool for dendritic TiC formation. Therefore, the morphology gradually transforms into short rod-like and black granular phases. During the solidification process of laser cladding, degradation of WC induced by the laser beam results in the priority formation of TiC reinforced phases due to the strong chemical affinity between Ti and C. This can be attributed to the active behavior of Ti, as it selectively incorporates C from the dissolving WC particles within the molten pool. The following reactions, estimated through free energy calculations, are based on the thermodynamic properties of WC and Ti [39,40]:

$$2WC+Ti \rightarrow W_2C+Ti \tag{2}$$

$$W_2C+T_1\rightarrow 2W+T_1C$$
 (3)

$$WC+Ti \rightarrow TiC+W$$
 (4)

The combined result of Reactions (2) and (3) is represented by Reaction (4). To further understand the microstructure formation mechanism in the coatings, the reaction model between WC and Ti-Al is illustrated in Fig. 6. As depicted in Fig. 6(a), pure Ti, Al, and WC are represented as spherical particles, with the WC particles uniformly mixed by the binder TiAl. Upon laser irradiation, an instantaneous input of high heat energy causes the melting of Ti, Al, and the base metal on the surface initially. With a further increase in temperature, simultaneous decarburization and dissolution of WC occur in the molten pool, forming W<sub>2</sub>C near the WC particles and complete reduction of residual WC particles, as shown in Fig. 6(b). Meanwhile, W and C atoms diffuse uniformly into the liquid,

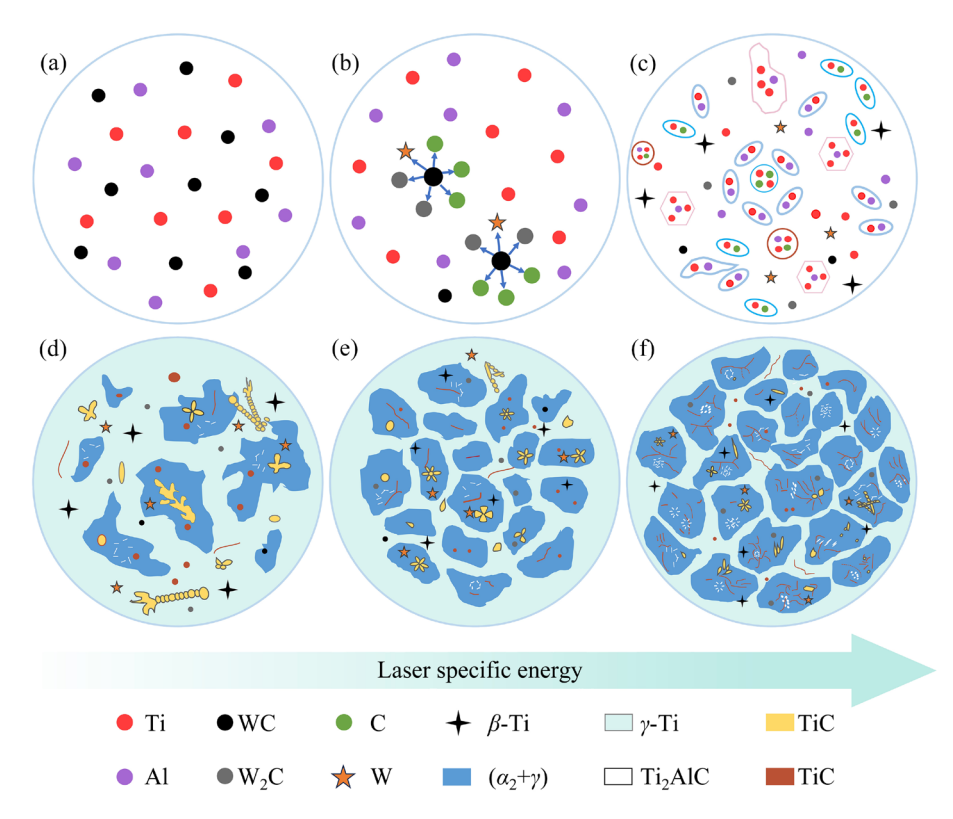


Fig. 6 Simplified diagram of microstructure formation mechanism for Ti-Al/WC coatings

reacting with other elements due to the stirring effect of the laser beam and convection within the molten pool (Fig. 6((c)). Furthermore, the formation of  $\alpha_2$ -Ti<sub>3</sub>Al and  $\gamma$ -TiAl microstructure occurred in the molten pool owing to the high affinity between Ti and Al atoms. During the solidification process of laser cladding, the hard TiC reinforced phase, which has a higher melting point and lower Gibbs free energy, preferentially precipitates in the molten pool. Meanwhile, as a crucial intermediate material in the formation of Ti<sub>2</sub>AlC, a portion of TiC can react with  $\gamma$ -TiAl to generate the ternary compound Ti<sub>2</sub>AlC phase. As the specific energy increased, the distribution of TiC tended to increase, the TiC thin strip tissue gradually intensified and the massive shape  $\gamma$ -TiAl became finer.

When the specific energy reached 116.7 J/mm<sup>2</sup>, the Ti<sub>2</sub>AlC phase and TiC reinforced phase were evenly distributed on the refined  $(\alpha_2+\gamma)$  matrix, as shown in Figs. 6(d-f). This can be attributed to further increased specific energy, leading to diffusion incorporation of Ti and Al atoms into TiC within the molten pool. Consequently, the thin strip TiC phase gradually converted to the Ti<sub>2</sub>AlC phase, refining the y-TiAl microstructure and promoting the continuous precipitation of white granular Ti<sub>2</sub>AlC phases. Generally, due to its complex lattice cell structure, Ti<sub>2</sub>AlC requires a high phase-forming diffusion activation energy, which is typically achieved at elevated temperatures [49]. Therefore, TiC phases preferred to form thin dendrites, and their quantity increased significantly, along with the Ti<sub>2</sub>AlC phase, as the specific energy increased from 66.7 to 116.7 J/mm<sup>2</sup>. As the temperature continued to drop and the molten pool solidified, small quantities of granular TiC emerged, possibly surrounded by  $\beta$ -Ti, which restricted their growth. These granular TiC can provide heterogeneous nucleation sites for  $\beta$ -Ti nucleation, helping to refine the  $(\alpha_2+\gamma)$  matrix. Moreover, Ti<sub>2</sub>AlC and  $\beta$ -Ti exhibit strong toughness, which mitigates stress concentrations of TiC and W2C, enhancing the wettability of coating and reducing crack defects.

#### 3.4 Microhardness

Figure 7 illustrates the microhardness distribution along the depth direction from the coating surface to the substrate, displaying varying microhardness values for different specific energy levels. Overall, a progressive declining trend in

microhardness distribution curves can be observed from the composite coatings to the substrate. The microhardness is relatively stable in the cladding zone, while it decreases rapidly in the bonding zone. Additionally, there is a slow decrease in microhardness from the heat affected zone to the substrate. Obviously, the cladding zone exhibits a remarkable increase in microhardness compared to the substrate owing to the dispersion distribution of the in-situ carbide reinforced phase in the cladding layer. It can be clearly observed that the microhardness of the coating at 66.7–100.0 J/mm<sup>2</sup> fluctuates significantly, possibly due to the uneven distribution of hard carbide caused by insufficient diffusion of C element. When the specific energy is increased to 116.7 J/mm<sup>2</sup>, the coating exhibits the highest microhardness and minimal fluctuation. This phenomenon can be attributed to the fact that microhardness is influenced not only by the microstructure of the coating but also by the specific energy. The increased laser energy and slower scanning speed prolong the molten state, allowing for the complete growth and flow of carbide in the molten pool. This is consistent with the transformation of TiC morphology into a thin strip phase, uniformly distributed in the microstructure in a uniform and dense form, as shown in Fig. 3(d).

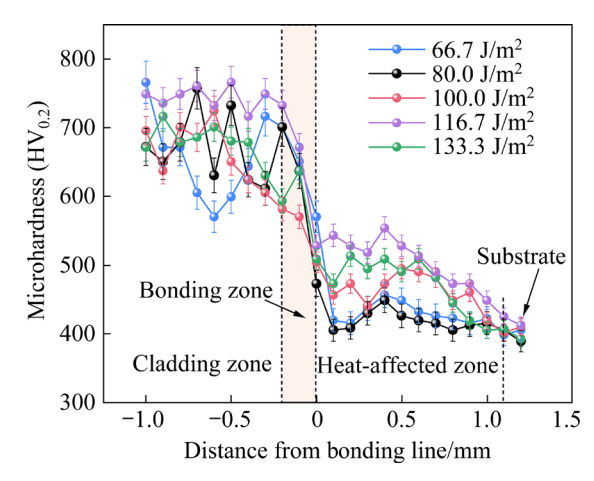


**Fig. 7** Microhardness distribution across cross-section of Ti–Al/WC coatings

The microhardness of the coating decreased significantly at a specific energy of 133.3 J/mm<sup>2</sup>, surpassing the critical value and causing violent interaction between the laser beam and molten pool, resulting in splashing of liquid droplets. This led to a reduction in carbide and other reinforcing phases

in the molten pool, while over-melting of the substrate further diluted the carbide content. At a specific energy was 116.7 J/mm<sup>2</sup>, the coating exhibited its highest microhardness at HV<sub>0.2</sub> 766.3, approximately 1.96 times higher than that of the substrate. However, at 133.3 J/mm<sup>2</sup>, the coating microhardness slightly decreased. This mainly attributed to the increased content of TiC, W<sub>2</sub>C, and Ti<sub>2</sub>AlC phases, which can improve the microhardness of the composite coatings. In the coating prepared at 116.7 J/mm<sup>2</sup>, which displayed the highest average microhardness, this can be attributed to the maximum content of the TiC thin strip phase and uniformly distributed Ti<sub>2</sub>AlC phase within the microstructure. Furthermore, TiC, acting as the core of heterogeneous nucleation, inhibits the growth in surrounding matrix phases and plays a role in the fine-grain strengthening during rapid cooling and solidification. High specific energy significantly increases the nucleation rate, precipitating the amount of uniformly dispersive Ti<sub>2</sub>AlC-TiC-dependent growth composite phases. This dispersion strengthening effectively improves the uniformity of the coating microstructure, resulting in a notable increase in microhardness. This can be ascribed to both the fine-grain strengthening of the  $(\alpha_2+\gamma)$  matrix and the interwoven structure of the Ti<sub>2</sub>AlC phase and TiC hard phase, which contribute to dispersion strengthening.

#### 3.5 Wear behavior analysis

In a dry sliding wear test at room temperature, the tribological characteristics of five coatings prepared with different specific energies were examined. The friction coefficient-time curves for both the substrate and Ti-Al/WC coatings are shown in Fig. 8. After conducting a wear test under identical conditions, it was observed that the friction coefficient of the coatings was significantly lower than that of the substrate, with the difference varing based on specific energy. During the initial wear period, the friction coefficient curve exhibited sharp fluctuations. Subsequently, there was a gradual increase in the friction coefficient for the substrate, indicating a notable rise in surface roughness and friction. The reason behind this lies in the initial wear stage when the contact surface had minimal roughness and engaged in point contact with the coated surface and Si<sub>3</sub>N<sub>4</sub> ball.

However, as the friction wear conducted, this interaction shifted from point contact to surface contact, resulting in increased resistance to grinding ball movement during the wear process, as reflected by an elevated friction coefficient. Nonetheless, the friction coefficient abruptly decreased after 25 min, possibly due to substrate pitting caused by mass peeling during the friction process.

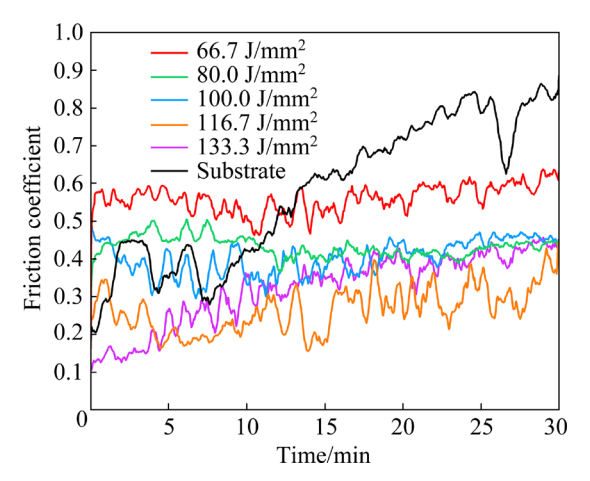


**Fig. 8** Friction coefficient—time curves of substrate and Ti–Al/WC coatings

As the specific energy increased, the friction coefficient of the coatings at the stable wear stage showed a negative correlation with microhardness, initially decreasing and then increasing. The friction coefficient values were also inversely correlated with the contents of TiC phase and Ti2AlC phase, as indicated by their diffraction peak intensities under varying heat inputs in Fig. 2. When the specific energy was increased to 116.7 J/mm<sup>2</sup>, Ti-Al/WC coating manifested a minimum friction coefficient. Considering the microstructure of the coatings, the friction coefficient may be influenced by the transformation of the TiC phase from dendritic fine to thin strip phase. These TiC network-reinforced structures act as rigid fulcrums in the coating, improving its bearing capacity and strength during wear. Furthermore, they act as the core for heterogeneous nucleation, generating more self-lubricating Ti<sub>2</sub>AlC white granules during cooling, inducing a pinning effect on the  $(\alpha_2+\gamma)$ TiAl matrix to increase the wear resistance of the coating. Therefore, it exhibits superior anti-wear performance.

Figure 9 demonstrates that the wear volume loss of the coatings follows the same trend as the friction coefficient for each sample. The wear rates

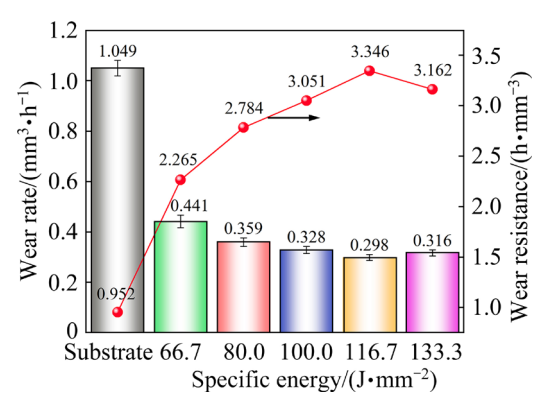


**Fig. 9** Effects of specific energy on wear rate and wear resistance of Ti–Al/WC coatings

of the substrate and coatings were approximately 1.049, 0.441, 0.359, 0.328, 0.298, and 0.316 mm<sup>3</sup>/h, respectively. Therefore, variations in microstructure tuning through specific energy can result in disparities in the wear resistance of Ti-Al/WC composite coatings. With the increase of specific energy, the wear rate initially decreases and then increases. Compared to the TC21 substrate, the wear rate of five coatings was reduced at room temperature. Notably, this reduction indicates an enhancement in wear resistance. The aforementioned results demonstrate that the coating exhibits optimal wear resistance at a specific energy of 116.7 J/mm<sup>2</sup>. The wear resistance (3.346 h/mm<sup>3</sup>) of the coating with a specific energy of 116.7 J/mm<sup>2</sup> was 3.52 times that of the substrate (0.952 h/mm<sup>3</sup>), indicating a remarkable improvement in its wear resistance, which correlates well with the friction coefficient curve. This is mainly attributed to the heterogeneous structure of the coating composed of refined ( $\alpha_2+\gamma$ ) TiAl matrix, hard TiC reticular-like structure, and self-lubricating Ti<sub>2</sub>AlC phase. This unique composition effectively impedes the plowing effect caused by grinding balls on the surface. However, it should be noted that when the specific energy reached 133.3 J/mm<sup>2</sup>, the wear resistance is slightly smaller than that of the coating prepared with a specific energy of 116.7 J/mm<sup>2</sup>, possibly due to a reduction in coating microhardness resulting from improved specific energy.

To further elucidate the underlying wear mechanisms associated with the substrate and coatings, the wear surface morphology of each analyzed through was microscopic characterization, with the test results presented in Fig. 10. Numerous debris particles and plowing furrows can be observed on the worn surface of the TC21 substrate, indicating significant wear induced by sliding friction, as shown in Fig. 10(a). In general, materials with lower hardness are more prone to adhesive wear. Over time, abrasive grains can be seen adhering to the material surface due to an increase in friction surface temperature, indicating that the primary wear mechanism of the substrate exhibits typical characteristics of both adhesive and abrasive wear. Comparatively, as the specific energy increased, wear debris on the surface of the coatings became progressively less pronounced, reducing the degree of spalling, as depicted in Figs. 10(b-e). The predominant wear mechanism of cladding coatings is abrasive wear. Furthermore, some isolated wear patches can be

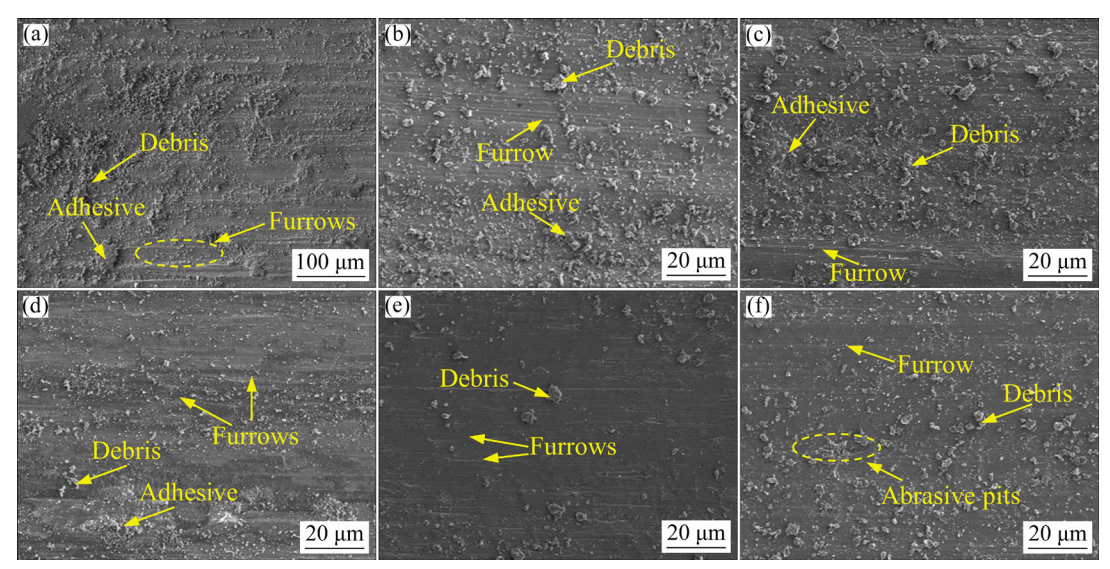


**Fig. 10** Worn surface morphologies of substrate (a) and Ti-Al/WC coatings prepared with different specific energies: (b) 66.7 J/mm<sup>2</sup>; (c) 80.0 J/mm<sup>2</sup>; (d) 100.0 J/mm<sup>2</sup>; (e) 116.7 J/mm<sup>2</sup>; (f) 133.3 J/mm<sup>2</sup>

seen in Figs. 10(b-d), indicating slight adhesion wear on the Ti-Al/WC coating prepared with a specific energy ranging from 66.7 to 100.0 J/mm<sup>2</sup>. The coexistence of adhesive and abrasive wear contributed to substantial wear loss in the coatings. Furrows were observed on the worn surface because of the enhanced hardness of the coating and formation of TiC hard phase. Under the applied load, abrasives were pressed into the friction surface, continuously slicing through and removing material from it. This induced a transition from two-body abrasive wear to three-body abrasive wear [50]. The  $\alpha_2$ -Ti<sub>3</sub>Al and  $\gamma$ -TiAl intermetallic compounds, along with the Ti<sub>2</sub>AlC phase in the cladding layer, exhibited good plastic toughness. This allowed them to release stress through deformation during friction, effectively improving the plowing resistance of the cladding layer. Furthermore, the existence of numerous solid solution atoms strengthened the deformation resistance of the cladding layer.

It is noteworthy that an abrasive wear morphology was present when the specific energy reached 116.7 J/mm<sup>2</sup>, and no noticeable adhesive wear characteristics were found at that point (Fig. 10(e)). This could be attributed to the tight combination of the  $(\alpha_2+\gamma)$  structure with the hard TiC reticular-like structure and self-lubricating Ti<sub>2</sub>AlC phase in the coatings, which reduced micro-cutting during grinding and resulted in only minor scratches. However, as specific energy continued to rise (as shown in Fig. 10(f)), a coarse worn surface and deposition of wear debris became visible again. The slight decrease in the microhardness of the coating, which resulted in reduced wear resistance, caused an increase in wear debris of the coating. In addition, at a specific energy of 133.3 J/mm<sup>2</sup> abrasive pits appeared on the coating surface during wear. This is mostly explained by the extreme thermal stress generated by excessively high laser irradiation. Simultaneously, uneven structures and stress concentrations may occur in the coating due to rapid heat transfer and solidification. When the stress during wear testing is above the critical value, hard phases separate from the  $(\alpha_2+\gamma)$  TiAl matrix, resulting in the emergence of abrasive pits. The friction mechanism from the double-body abrasive wear changed owing to the shedding of the hard phases, which eventually lowered the wear resistance of the coating. The above analysis indicates that the coating prepared with 116.7 J/mm<sup>2</sup> exhibits superior wear resistance. Furthermore, a dense network structure was formed by coupling thin-strip shape TiC with white granular phase Ti<sub>2</sub>AlC. This not only effectively helps to restrict the fluctuation range of the friction curve during the stable period but also ameliorates the surface roughness and shear deformation, thereby enhancing tribological performance and making the coating suitable for severe wear conditions.

# 4 Conclusions

- (1) The Ti–Al/WC composite coating was primarily composed of TiC hard phases, intermetallic compounds,  $\alpha_2$ -Ti<sub>3</sub>Al,  $\gamma$ -TiAl, and Ti<sub>2</sub>AlC phases, along with minor amounts of  $\beta$ -Ti, W<sub>2</sub>C and WC phases.
- (2) As the specific energy increased, the microstructure was gradually refined. At a specific energy of  $116.7 \text{ J/mm}^2$ , the smaller-size intermetallic compounds of  $\alpha_2$ -Ti<sub>3</sub>Al and  $\gamma$ -TiAl became denser, and numerous TiC thin strip phases were evenly dispersed in the coating to form a reticular-like structure.
- (3) Compared to the TC21 substrate, the Ti–Al/WC composite coatings exhibited higher microhardness. The microhardness distribution showed a gradient decrease from the cladding coating to the heat affected zone and then to the substrate. The drastic improvement in microhardness can be attributed to the combined effects of fine-grained strengthening of the  $(\alpha_2+\gamma)$  matrix and dispersion strengthening, which arise from the interwoven structure of the Ti<sub>2</sub>AlC and TiC hard phases.
- (4) The composite coating prepared with a specific energy of 116.7 J/mm<sup>2</sup> exhibited the best wear resistance, which was 3.52 times that of the substrate. Laser cladding shows significant potential for enhancing the wear resistance of titanium alloys through surface treatment. Moreover, Ti–Al/WC coatings prepared with specific energies ranging from 66.7 to 100.0 J/mm<sup>2</sup> exhibited high wear mass loss owing to the coexistence of adhesive and abrasive wear.

# CRediT authorship contribution statement

Xin-meng SUI: Conceptualization, Methodology,

Investigation, Writing — Original draft, Funding acquisition; **Yi-tao WENG:** Formal analysis, Writing — Review & editing, Software, Funding acquisition; **Jian LU:** Methodology, Funding acquisition, Writing — Review & editing, Supervision; **Lin ZHANG:** Methodology, Investigation, Software, Visualization; **Wei-ping ZHANG:** Resources, Writing — Review & editing, Supervision, Project administration.

# **Declaration of competing interest**

The authors declare that they have no known competing financial interests or personal relationships that could have appeared to influence the work reported in this paper.

#### Acknowledgments

This work was supported by the Guangxi Science and Technology Program, China (Nos. Guike AD23026170, Guike AD23026116), the Guangxi Key Laboratory of Manufacturing System and Advanced Manufacturing Technology, China (No. 22-35-4-S019), the Research Basic Ability Enhancement Program for Middle-aged Teachers of Guangxi, China (No. 2023KY0202), China Postdoctoral Science Foundation (No. 2024M753642), the Guilin Science and Technology Development Program (Project), China (No. 20220124-10), and the Innovation Project of GUET Graduate Education, China (No. 2024YCXS008).

#### References

- LI Qiang, HUANG Sheng, ZHAO Ya-kai, GAO Yi-min, RAMAMURTY U. Simultaneous enhancements of strength, ductility, and toughness in a TiB reinforced titanium matrix composite [J]. Acta Materialia, 2023, 254: 118995.
- [2] TIAN Yu-xin, XIAO Hua-qiang, YOU Chuan-chuan, FENG Jin-yu, XIAO Yi, ZHOU Xuan. High-temperature oxidation and wear properties of laser cladded Ti-Al-N composite coatings [J]. Transactions of Nonferrous Metals Society of China, 2023, 33: 1779–1791.
- [3] BAI Yan-yun, XI Ye-ting, GAO Ke-wei, YANG Hui-sheng, PANG Xiao-lu, VOLINSKY A A. Residual stress control in CrAlN coatings deposited on Ti alloys [J]. Ceramics International, 2018, 44: 4653–4659.
- [4] ZHAO Qin-yang, SUN Qiao-yan, XIN She-wei, CHEN Yong-nan, WU Cong, WANG Huan, XU Jian-wei, WAN Ming-pan, ZENG Wei-dong, ZHAO Yong-qing. High-strength titanium alloys for aerospace engineering applications: A review on melting-forging process [J]. Materials Science and Engineering A, 2022, 845: 143260.
- [5] HUA Ke, DING Hai-tao, SUN Ling-hong, CAO Yue, LI Xiao-lin, WU Hong-xing, WANG Hai-feng. Enhancing high-temperature fretting wear resistance of TC21 titanium alloys by laser cladding self-lubricating composite coatings [J]. Journal of Alloys and Compounds, 2024, 977: 173360.
- [6] ZHANG Qiang, CHEN Jing, GUO Peng-fei, TAN Hua, LIN

- Xin, HUANG Wei-dong. Texture and microstructure characterization in laser additive manufactured Ti-6Al-2Zr-2Sn-3Mo-1.5Cr-2Nb titanium alloy [J]. Materials & Design, 2015, 88: 550-557.
- [7] ZHU Yan-song, LIU Yun-fei, WEI Xing-nong, SUN Dong, LU Wen-zhuang, KO Tae-jo. Tribological characteristics of the dual titanium boride layers (TiB<sub>2</sub>+TiB) on titanium alloy [J]. Ceramics International, 2021, 47: 13957–13969.
- [8] ZHOU Kai, XIE Fa-qin, WU Xiang-qing, WANG Shao-qing. Fretting wear behavior of nano ZrO<sub>2</sub> doped plasma electrolytic oxidation composite coatings on TC21 titanium alloy [J]. Surface and Coatings Technology, 2021, 421: 127429.
- [9] WANG, Jiang-xiong, YE Xian-wei, LI Yuan-hui, WAN Ming-pan, HUANG Chao-wen, HUANG Fang, LEI Min, LIU Dan, MA Rui, REN Xian-li. Effect of annealing temperature on mechanical properties of TC21 titanium alloy with multilevel lamellar microstructure [J]. Materials Science and Engineering A, 2023, 869: 144788.
- [10] YUAN Bao-guo, TANG Ai-chuang, QIAN De-guo, CHEN Qiang, ZHANG Xiao-xue, HUANG Zhong-yue. Roomtemperature compressive properties of TC21 alloy processed by thermohydrogen treatment at 1123 K [J]. International Journal of Hydrogen Energy, 2022, 47: 25066–25079.
- [11] WANG M, DU L, XU Y, ZHANG X, QI P T, XU P, PENG W H. Surface microstructure evolution mechanism of WC-Co hard alloy treated by high current pulsed electron beam [J]. Vacuum, 2022, 202: 111139.
- [12] LU Jian, SUI Xin-meng, NOVOSELOV Kostya S., HUANG Peng-ru, XU Fen, SUN Li-xian. Electron beam-assisted synthesis and modification of electrode/separator materials for lithium-ion batteries: Progress and prospects [J]. Coordination Chemistry Reviews, 2024, 515: 215954.
- [13] YUMUSAK G, LEYLAND A, MATTHEWS A. A microabrasion wear study of nitrided α-Ti and β-TiNb PVD metallic thin films, pre-deposited onto titanium alloy substrates [J]. Surface and Coatings Technology, 2022, 442: 128423.
- [14] SITEK R, KAMINSKI J, BORYSIUK J, MATYSIAK H, KUBIAK K, KURZYDLOWSKI K J. Microstructure and properties of titanium aluminides on Ti6Al4V titanium alloy produced by chemical vapor deposition method [J]. Intermetallics, 2013, 36: 36–44.
- [15] LI Run-guang, WANG You-kang, XU Ning, YAN Zhi-ran, LI Shi-lei, ZHANG Ming-he, ALMER J, REN Yang, WANG Yan-dong. Unveiling the origins of work-hardening enhancement and mechanical instability in laser shock peened titanium [J]. Acta Materialia, 2022, 229: 117810.
- [16] FENG Jing, WANG Jun, YANG Kai-long, RONG Ju. Microstructure and performance of YTaO<sub>4</sub> coating deposited by atmospheric plasma spraying on TC4 titanium alloy surface [J]. Surface and Coatings Technology, 2022, 431: 128004.
- [17] LI Gang-qiang, MA Feng-cang, LIU Ping, QI Sheng-cai, LI Wei, ZHANG Ke. Review of micro-arc oxidation of titanium alloys: Mechanism, properties and applications [J]. Journal of Alloys and Compounds, 2023, 948: 169773.
- [18] YANG Xin, WANG Wan-lin, MA Wen-jun, WANG Yan, YANG Jun-gang, LIU Shi-feng, TANG Hui-ping. Corrosion and wear properties of micro-arc oxidation treated Ti6Al4V

- alloy prepared by selective electron beam melting [J]. Transactions of Nonferrous Metals Society of China, 2020, 30: 2132–2142.
- [19] SUI Xin-meng, LU Jian, ZHANG Xian, SUN Lin, ZHANG Wei-ping. Microstructure and properties of TiC-reinforced Ti<sub>2</sub>Ni/Ti<sub>5</sub>Si<sub>3</sub> eutectic-based laser cladding composite coating [J]. Journal of Thermal Spray Technology, 2020, 29: 1838–1846.
- [20] HONG S H, EO D R, LEE S, CHO J W, KIM S J. Strong resistance to Zn-assisted liquid metal embrittlement of austenitic-TWIP/martensitic-HSLA multi-layered steel sheets additively manufactured by laser cladding [J]. Acta Materialia, 2023, 258: 119224.
- [21] LIU Yue-yang, YANG Yang, CHEN Chao. Microstructure and properties of Ni-Ti based gradient laser cladding layer of Ti6Al4V alloy by laser powder bed fusion [J]. Additive Manufacturing, 2024, 79: 103906.
- [22] GOPINATH M, MULLICK S, NATH A K. Development of process maps based on molten pool thermal history during laser cladding of Inconel 718/TiC metal matrix composite coatings [J]. Surface and Coatings Technology, 2020, 399: 126100.
- [23] ZHU Li-da, XUE Peng-sheng, LAN Qing, MENG Gui-ru, REN Yu-an, YANG Zhi-chao, XU Pei-hua, LIU Zhe. Recent research and development status of laser cladding: A review [J]. Optics & Laser Technology 2021, 138: 106915.
- [24] ZHAO Yi-tian, LU Ming-yuan, FAN Zhi-qi, HUANG Shui-quan, HUANG Han. Laser deposition of wear-resistant titanium oxynitride/titanium composite coatings on Ti-6Al-4V alloy [J]. Applied Surface Science, 2020, 531: 147212.
- [25] ZHANG Yong-shi, LIU Zhen-guang, LV Zhong-hui, CAO Jia-wen, TONG Ying-jie, SUN Ming-yan, CUI Chen-shuo, WANG Xiao-nan. Effect of SiC and TiC content on microstructure and wear behavior of Ni-based composite coating manufactured by laser cladding on Ti-6Al-4V [J]. Wear, 2024, 552/553: 205431.
- [26] SUI Xin-meng, LU Jian, WEI De-qiang, ZHANG Lin, WANG Rong, ZHAO Wei, ZHANG Wei-ping. Unveiling the influence of TiN on the microstructure and high-temperature oxidation behavior of Ti-Al-Cr composite coating [J]. Corrosion Science, 2022, 206: 110539.
- [27] LI Jian, CUI Xiu-fang, GUAN Ya-jie, JIN Guo, ZHENG Wei, LIU Er-bao, WAN Si-min, SHI Zi-zhong. Effect of SiC content on microstructural evolution and tribology properties of laser-clad TiC-reinforced Ti-Al-Si composite coatings [J]. Materials Today Communications, 2023, 35: 106019.
- [28] WANG Xiang, ZHANG Lin-jie, NING Jie, LI Sen, ZHANG Liang-liang, LONG Jian. Hierarchical grain refinement during the laser additive manufacturing of Ti-6Al-4V alloys by the addition of micron-sized refractory particles [J]. Additive Manufacturing, 2021, 45: 102045.
- [29] ZHAO Yi-tian, LU Ming-yuan, FAN Zhi-qi, MCCORMICK Paul, TAN Qi-yang, MO Ning. Microstructures and mechanical properties of wear-resistant titanium oxide coatings deposited on Ti-6Al-4V alloy using laser cladding [J]. Journal of the European Ceramic Society, 2020, 40: 798-810.
- [30] JIANG Chao-ping, ZHANG Jun, CHEN Yong-nan, HOU

- Zhi-min, ZHAO Qin-yang, LI Yao, ZHU Li-xia, ZHANG Feng-ying, ZHAO Yong-qing. On enhancing wear resistance of titanium alloys by laser cladded WC–Co composite coatings [J]. International Journal of Refractory Metals and Hard Materials, 2022, 107: 105902.
- [31] DAI Jing-jie, ZHU Ji-yun, CHEN Chuan-zhong, WENG Fei. High temperature oxidation behavior and research status of modifications on improving high temperature oxidation resistance of titanium alloys and titanium aluminides: A review [J]. Journal of Alloys and Compounds, 2016, 685: 784–798.
- [32] WU Qi-long, LONG Wei-min, ZHANG Lei, ZHAO Hong-wei. A review on ceramic coatings prepared by laser cladding technology [J]. Optics and Laser Technology, 2024, 176: 110993.
- [33] PAN Cheng-gang, FANG Cheng-jie, SHI Ji, MA Kai-jiang, YANG Hui, HE Peng. Synthesis and properties of Ti–Al coating by high-frequency induction heated combustion [J]. Journal of Alloys and Compounds, 2023, 939: 168739.
- [34] DENG Qing-chen, WANG Xing-chen, LAN Qiao, CHANG Zhi-yu, LIU Ze-hua, SU Ning, WU Yu-juan, LIU Da-zhi, PENG Li-ming, DING Wen-jiang. Limitations of linear energy density for laser powder bed fusion of Mg-15Gd-1Zn-0.4Zr alloy [J]. Materials Characterization, 2022, 190: 112071.
- [35] YOU A-peng, WANG Nan, CHEN Yong-nan, JIANG Chao-ping, ZHANG Ying, ZHAO Qin-yang, SHI Ying, LI Yao, ZHANG Feng-ying, ZHAO Yong-qing. Effect of linear energy density on microstructure and wear resistance of WC-Co-Cr composite coating by laser cladding [J]. Surface & Coatings Technology, 2023, 454: 129185.
- [36] SUI Xin-meng, LU Jian, HU Ji, ZHANG Wei-ping. Effect of specific energy on microstructure and properties of laser cladded TiN/Ti<sub>3</sub>AlN-Ti<sub>3</sub>Al composite coating [J]. Optics & Laser Technology, 2020, 131: 106428.
- [37] WENG Fei, YU Hui-jun, CHEN Chuan-zhong, LIU Jian-li, ZHAO Long-jie, DAI Jing-jie, ZHAO Zhi-huan. Effect of process parameters on the microstructure evolution and wear property of the laser cladding coatings on Ti-6Al-4V alloy [J]. Journal of Alloys and Compounds, 2017, 692: 989–996.
- [38] KUMAR S, MANDAL A, DAS A K. The effect of process parameters and characterization for the laser cladding of cBN based composite clad over the Ti6Al4V alloy [J]. Materials Chemistry and Physics, 2022, 288: 126410.
- [39] QI Chao-qi, ZHAN Xiao-hong, GAO Qi-yu, LIU Li-jun, SONG Yuan-zeng, LI Ya-ping. The influence of the pre-placed powder layers on the morphology, microscopic characteristics and microhardness of Ti-6Al-4V/WC MMC coatings during laser cladding [J]. Optics and Laser Technology, 2019, 119: 105572.
- [40] CHEN Yan-bin, LIU De-jian, LI Li-qun, LI Fu-quan. Microstructure evolution of single crystal WC<sub>p</sub> reinforced Ti-6Al-4V metal matrix composites produced at different cooling rates [J]. Journal of Alloys and Compounds, 2009, 484: 108-112.
- [41] ZHANG Xin-jie, CUI Hong-zhi, WANG Jia-feng, ZHANG Guo-song, ZHAO Yu-qiao, SUN Kang. Effects of TiB<sub>2</sub>+TiC content on microstructure and wear resistance of Ni55-based composite coatings produced by plasma cladding [J].

- Transactions of Nonferrous Metals Society of China, 2019, 29: 132-142.
- [42] LUO Xi-li, ZHANG Kai-kai, CAO Jing, MENG Guang-hui, YU Fang-li, ZHOU Ying-ying, ZHOU Hong-wei, LA Pei-qing, XIE Hui. Effect of line energy density of the laser beam on the microstructure and wear resistance properties of the obtained Fe<sub>3</sub>Al laser cladding coatings [J]. Optik, 2022, 261: 169256.
- [43] XIAO Yi, XIAO Hua-qiang, FENG Jin-yu, LIN Bo, WANG Ying. Core-shell ZrC/Ti<sub>2</sub>AlC reinforced composite coatings prepared by laser cladding on Zr-alloy substrates [J]. Ceramics International, 2022, 48: 8136–8142.
- [44] TIAN Yu-xin, XIAO Hua-qiang, REN Li-rong, FENG Jin-yu, XIAO Yi, CHEN Nuo, ZHOU Xuan. A new strategy to fabricate Ti<sub>2</sub>AlC MAX coatings by the two-step laser method [J]. Surface & Coatings Technology, 2022, 448: 128944.
- [45] YANG Wei-gang, LI Ming-ao, ZHOU Tao, HU Li, SHI Lai-xin, XIAO Shu-long, CHEN Yu-yong. Deformation behavior and dynamic recrystallization mechanism of a novel high Nb containing TiAl alloy in (α+γ) dual-phase field [J]. Journal of Alloys and Compounds, 2023, 945: 169250.
- [46] KUMAR R R, CUPTA R K, PRASAD M J N V. Interface

- microstructure and mechanical response of similar and dissimilar joints of  $(\gamma+\alpha_2)$  titanium aluminide and  $\alpha$ -titanium alloy produced by diffusion bonding [J]. Materials Today Communications, 2023, 37: 107167.
- [47] ZHANG Lin, ZHAO Wei, SUI Xin-meng, ZHANG Wei-ping. Research on microstructure and properties of laser cladding Ti-Al/WC coating on titanium alloy [J]. Hot Working Technology, 2023, 52: 108–113. (in Chinese)
- [48] JIN Yun-xue, LI Jun-gang. Study of morphology and preferentially growing direction of TiC crystal in titanium alloy [J]. Titanium Industry Progress, 2005(3): 25–28. (in Chinese)
- [49] GO T, SOHN Y J, MAUER G, VAβEN R, JULIAN G. Cold spray deposition of Cr<sub>2</sub>AlC MAX phase for coatings and bond-coat layers [J]. Journal of the European Ceramic Society, 2019, 39: 860–867.
- [50] ZHAO Xin, LU Xin, ZUO Han-ning, MA Shuo-chen, WANG Chang, LI M V. TiBw reinforced titanium matrix composites fabricated by selective laser melting: Influence of energy density on microstructure and tribological performance [J]. Ceramics International, 2023, 49: 28920–28933.

# 激光比能量对高性能 Ti-AI/WC 复合涂层摩擦学性能的影响机理

隋欣梦<sup>1,2</sup>, 翁奕涛<sup>2</sup>, 卢健<sup>2,3</sup>, 张林<sup>1</sup>, 张维平<sup>1</sup>

- 1. 大连理工大学 材料科学与工程学院 辽宁省凝固控制与数字化制备技术重点实验室, 大连 116024;
  - 2. 桂林电子科技大学 机电工程学院 广西制造系统与先进制造技术重点实验室, 桂林 541004;
  - 3. 中国有色桂林矿产地质研究院有限公司 国家特种矿物材料工程技术研究中心,桂林 541004

摘 要:激光比能量对复合涂层的质量有重要影响。采用激光熔覆技术在 TC21 合金表面制备 Ti-Al/WC 涂层,激光比能量为  $66.7\sim133.3~\mathrm{J/mm^2}$ 。结果表明,复合涂层主要由 Ti<sub>2</sub>AlC、 $\alpha_2$ -Ti<sub>3</sub>Al、 $\gamma$ -TiAl、TiC 和 W 相组成。随着比能量的增大,Ti<sub>2</sub>AlC、 $\alpha_2$ -Ti<sub>3</sub>Al 和 TiC 衍射峰的相对强度逐渐升高。当比能量为  $116.7~\mathrm{J/mm^2}$ 时,Ti-Al/WC 涂层合金的最大显微硬度为  $HV_{0.2}$  766.3,与 TC21 合金相比硬度提高了  $1.96~\mathrm{G}$ ,最小磨损率大幅降低。通过( $\alpha_2$ + $\gamma$ )基体的细晶强化以及自润滑 Ti<sub>2</sub>AlC 与 TiC 相交织形成的弥散强化,摩擦学性能得到显著提升。该研究为高性能 Ti-Al 复合涂层的发展提供有价值的参考。

关键词: 激光比能量; Ti-Al/WC 涂层; TC21 合金; Ti<sub>2</sub>AlC; 摩擦学性能

(Edited by Bing YANG)